PHYSICAL REVIEW A **94**, 042707 (2016)

B-spline *R*-matrix-with-pseudostates approach for excitation and ionization of atomic oxygen by electron collisions

S. S. Tayal[1,*] and Oleg Zatsarinny[2,†]
[1]*Department of Physics, Clark Atlanta University, Atlanta, Georgia 30314, USA*
[2]*Department of Physics and Astronomy, Drake University, Des Moines, Iowa 50311, USA*

(Received 15 August 2016; published 21 October 2016)

Electron scattering with atomic oxygen has been studied using the B-spline R-matrix-with-pseudostates method. Cross sections for elastic scattering, excitation, emission, and ionization processes are presented. The excitation cross sections have been calculated for transitions between the $2s^22p^4$ and $2s^22p^33l$ states of oxygen in the energy range from threshold to 200 eV. The present work differs from numerous previous studies due to the inclusion of a large number of pseudostates in the calculation. We included a total of 1116 spectroscopic bound, core-excited autoionizing, and target continuum states in the close-coupling expansion. The atomic oxygen structure model has been described by combining the multiconfiguration Hartree-Fock and the B-spline box-based multichannel methods. The inclusion of a large number of pseudostates representing the target continuum has a major impact, especially on the theoretical prediction of the excitation cross sections for many transitions at intermediate energies. A large reduction in excitation and emission cross sections has been noted due to the inclusion of coupling to the ionization continuum. The calculated cross sections are now in better agreement with available experimental results. The ionization cross sections for the ground $2s^2\,2p^4\,{}^3P$ and metastable $2s^22p^4\,{}^1D$ and ${}^1S$ states are also presented. The electron-impact-induced emission cross sections for the $(2s^22p^33s)\,{}^3S^o$–$(2s^22p^4)\,{}^3P$ (130.4 nm), $(2s^22p^33d)\,{}^3D^o$–$(2s^22p^4)\,{}^3P$ (102.7 nm), $(2s^22p^33s')\,{}^3D^o$–$(2s^22p^4)\,{}^3P$ (98.9 nm), and $(2s^22p^33s'')\,{}^3D^o$–$(2s^22p^4)\,{}^3P$ (87.8 nm) transitions have been calculated and compared with the available experimental results.

DOI: 10.1103/PhysRevA.94.042707

I. INTRODUCTION

Theoretical studies of electron scattering from the open p-shell atoms including atomic oxygen are of special interest because of the importance of short-range correlation effects in the target description and long-range polarization effects in the scattering approach. Inclusion of coupling to the ionization continuum and quasidiscrete states is essential for electron scattering from atomic oxygen. Accurate energy levels, oscillator strengths, and cross sections for electron collisions with atomic oxygen are of great importance in the modeling of various astrophysical plasmas. Strong emission lines of oxygen have been observed in the spectra from chromospheres and transition regions of the Sun and cool stars [1,2]. The intensity ratios of several of these lines offer good temperature and density diagnostics of the solar and planetary atmospheres. The electron-induced emission cross sections for the atomic-oxygen 130.4-nm multiplet due to excitation of the $(2s^22p^33s)\,{}^3S^o$ state are very important for the understanding of the interaction between Io's local and extended atmospheres and Jupiter's magnetosphere [3]. The atomic oxygen and sulfur are the primary species in Io's atmosphere and neutral clouds. Oscillator strengths and electron impact excitation cross sections are needed for the atomic oxygen multiplets at 130.4, 102.7, 98.9, 87.8, and 79.2 nm due to the $(2s^22p^4)\,{}^3P$–$(2s^22p^33s)\,{}^3S^o$, $(2s^22p^4)\,{}^3P$–$(2s^22p^33d)\,{}^3D^o$, $(2s^22p^4)\,{}^3P$–$(2s^22p^33s')\,{}^3D^o$, $(2s^22p^4)\,{}^3P$–$(2s^22p^33s'')\,{}^3D^o$, and $(2s^22p^4)\,{}^3P$–$(2s2p^5)\,{}^3P^o$ resonance transitions, respectively, for modeling of astrophysical plasmas. The oxygen abundances are useful for the understanding of the chemical evolution of stars and galaxies. The excitation of the $(2s^22p^33p)\,{}^5P$ multiplet gives rise to 777-nm lines which offer good oxygen abundance diagnostics in the atmospheres of F, G, and K-type stars [4]. Oxygen abundances and abundance ratios with iron are important to understand stellar structure and evolution due to the importance of the CNO nucleosynthesis cycle and oxygen large opacity [4,5]. Oxygen abundances play a role in understanding the chemistry of exoplanetary atmospheres [6].

There is a large number of both experimental and theoretical studies for the excitation of atomic oxygen by electron impact. The cross sections from these studies have been reviewed by Johnson *et al.* [7], showing that the agreement between theories and experiments varies for different transitions and energy regions. The details of the previous theoretical and experimental works can also be found in the paper by Johnson *et al.* [7]. Earlier calculations for the excitation cross sections may be uncertain because the important coupling to the target continuum was ignored. As shown by numerous studies, this coupling may significantly affect the cross sections at intermediate energies above the ionization threshold. Especially it is true with the atoms where the continuum makes significant contributions to the polarizability of low-lying states. Oxygen is a typical example of such cases where 75% of the polarizabilities of the $2s^22p^4$ ground-configuration states come from the continuum.

Zatsarinny and Tayal [8,9] investigated cross sections for the excitation of the $3s\,{}^3S^o$, $3s\,{}^3D^o$, $3s'\,{}^3D^o$, $3s''\,{}^3P^o$, and $2s2p^5\,{}^3P^o$ states by electron impact using a 26-state B-spline R-matrix approximation in the energy region from threshold to 100 eV. They first used the term-dependent nonorthogonal one-electron radial functions for accurate representation of the

---

[*] stayal@cau.edu

[†] oleg.zatsarinny@drake.edu

target states. They additionally carried out 8-state, 16-state, and 22-state calculations to check the convergence of the close-coupling expansions. More recently, Tayal [10,11] performed 52-state, 41-state, and 34-state R-matrix-with-pseudostates (RMPS) calculations with orthogonal orbitals for the resonance transitions to investigate the importance of coupling to the continuum. It was estimated that the contribution of the ionization continuum to the cross section varies from 5% to 15% for the excitation of the ${}^3P$–$3s\,{}^3S^o$ transition. A limited number of pseudostates, however, does not allow to make a definitive assessment of the calculated cross sections. Plummer *et al.* [12] used the RMATRIXII computer package to perform six-state calculations with various sets of basis functions to calculate elastic cross sections for the $2p^4\,{}^3P$ ground state and excitation cross sections to and between the $2p^4\,{}^1D$ and ${}^1S$ states. The six-state calculations included three target states $2p^4\,{}^3P$, ${}^1D$, ${}^1S$ and three long-range polarization pseudostates. They also performed 6-state, 12-state, 169-state, and 191-state test calculations using a systematic radial basis.

The purpose of the present paper is to fully investigate the importance of coupling to the continuum and to extend the previous calculations further and thereby to provide an ultimate assessment for the likely accuracy of the available collision data for atomic oxygen. It seems highly appropriate to carry out much larger calculations than what was not possible just a few years ago and to provide a complete and consistent set of scattering data which include the elastic scattering, emission, excitation, and ionization processes. The present work is a part of a series of extensive pseudostate calculations for electron scattering from atoms with a partially or fully occupied $2p$ outer shell, such as C [13], N [14], F [15], and Ne [16,17]. As shown in these studies, coupling to the ionization continuum and, albeit to a smaller extent, the higher-lying discrete Rydberg spectrum as well as autoionizing states can have a major effect on theoretical predictions for electron-induced transitions including both optically allowed and forbidden transitions. Along with the need for accurate representation of target states, adequate accounting for the target continuum is a crucial condition for obtaining accurate scattering cross sections. The ground state of oxygen has an open $2p^4$ shell, and due to statistical considerations atomic oxygen has a much more dense spectrum than other $2p$-shell atoms mentioned above. In order to treat oxygen at the same level of accuracy, we thereby need to include a much larger number of target pseudostates.

The present calculations have been carried out with the B-spline R-matrix (BSR) suite of codes [18], which is a general computer codes package that can be applied to complex open-shell targets. In recent years we have extended these codes in several ways; the ability to include and handle a large number of pseudostates in the close-coupling expansion is the most important update of the codes. The pseudostates are of finite range and hence represent discrete-level approximations of the high-lying Rydberg series states and the ionization continuum. Though the coupling to the target continuum cannot be accounted for exactly, the pseudostates provide a sufficiently accurate representation of the basic effect. In addition, the pseudostates allow for the calculation of ionization process. Compared to the other widely used R-matrix codes [19,20], the BSR approach allows for the use of nonorthogonal orbital sets. The nonorthogonal orbitals provide greater flexibility in the description of the target states and more accurate account of correlation effects. However, there is a significant increase in the complexity of setting up the Hamiltonian matrix and, consequently, the requirement of computational resources. On the other hand, a much improved target description results in more reliable and accurate scattering cross sections. The continuum pseudostates in our approach are generated from the direct diagonalization of the atomic Hamiltonian in the multichannel B-spline basis. It provides a rigorous description of low-energy quasidiscrete states in the continuum, and in combination with the projection technique also allows us to consider such highly correlated processes as ionization plus excitation [21,22].

In this paper we summarize the most important features of the present model for the e-O scattering process in Sec. II. After summarizing the computational details of structure and scattering calculations in Sec. II, we present the results in Sec. III together with discussion of our results and a comparison with available previous calculations and experimental data. Besides elastic momentum-transfer cross sections and results for state-selective excitation processes as well as electron-impact ionization, we also include results for elastic scattering, the sum of all inelastic excitations, superelastic deexcitation (in case the initial state is not the ground state), and ionization to form the so-called grand total cross sections. We focus our discussion on the excitation of the forbidden transitions within the states of ground configuration, resonance transitions to several excited states, as well as excitation of the $2p^33s\,{}^5S^o$ and $2p^33p\,{}^5P$ states giving rise to lines in the observed spectra of numerous astrophysical objects. We present our results in a form that might be useful for astrophysical plasma applications. A brief summary and conclusions are presented in Sec. IV.

II. METHODS OF CALCULATIONS

A. Target wave functions

We used a combination of the multiconfiguration Hartree-Fock (MCHF) and the B-spline box-based close-coupling methods [23] to generate atomic oxygen target states. The structure of the multichannel target expansion in this approach was chosen as

$$\begin{aligned}\Phi(2s^22p^3nl,LS) = &\sum_{nl,L'S'}\{\phi(2s^22p^3,L'S')P(nl)\}^{LS}\\ &+\sum_{nl,L'S'}\{\phi(2s2p^4,L'S')P(nl)\}^{LS}\\ &+a\varphi(2s^22p^4)^{LS}+b\varphi(2s2p^5)^{LS},\end{aligned}\quad (1)$$

where the functions of the outer valence electrons are denoted by $P(nl)$, while the ϕ and φ functions represent the configuration-interaction (CI) expansions of the corresponding ionic or specific atomic states, respectively. These expansions were generated in separate MCHF calculations for each state using the MCHF program [24].

The above expansion (1) represents a model for the entire $2s^22p^3nl$ and $2s2p^4nl$ Rydberg series of bound and autoionizing states in neutral oxygen, including the continuum pseudostates lying above the ionization limit. The first two sums in this expansion can also provide a good approximation for states with equivalent electrons, namely, for all terms of the ground-state configuration $2s^22p^4$ as well as for the core-excited states $2s2p^5$. We found, however, that it is more appropriate to employ separate CI expansions for these states by directly including relaxation and term-dependence effects via state-specific one-electron orbitals.

We have included the inner-core or short-range correlation effects through the CI expansions of the $2s^22p^3$ and $2s2p^4$ ionic states. These expansions include all single and double excitations from the $2s$ and $2p$ orbitals to the $3l$ and $4l$ ($l = 0$–3) correlated orbitals. We generated these orbitals for each state separately. The final expansions for the atomic states were kept to a reasonable size by dropping all configurations with coefficients of less than 0.01 from the CI expansions. The resulting ionization potentials for all ionic states agreed with experiment [25] to within 0.01 eV.

The outer valence electron functions $P(nl)$ were expanded in a B-spline basis, and the corresponding multichannel close-coupling equations were solved by imposing the condition that the orbitals vanish at the boundary. The R-matrix radius was set to $25a_0$, where $a_0 = 0.529 \times 10^{-10}$ m is the Bohr radius. We employed 55 B splines of order 8 to span this radial range using a semiexponential knot grid. The B-spline coefficients for the valence electron functions $P(nl)$ and the coefficients a and b for the perturbers were obtained by diagonalizing the nonrelativistic LS atomic Hamiltonian. The B-spline bound-state close-coupling calculations generate different nonorthogonal sets of orbitals for each atomic state, and their subsequent use in scattering calculations is somewhat complicated. Our configuration expansions for the atomic target states contained from 50 to 200 configurations for each state. These configurations are manageable in the subsequent large-scale collision calculations with the available computational resources.

In Table I we compare the present calculated energies of oxygen with the values of the LS multiplets listed in the NIST Atomic Levels and Spectra database [25]. The overall agreement between our results and the NIST database is satisfactory. The deviations in the calculated energy splitting from the NIST values are generally less than 0.1 eV for most states. The larger deviation of 0.15 eV is observed only for the $2p^33s$ states. For these states larger corrections are expected due to core-valence correlation which was not included in our target expansions to a full extent due to limited BSR expansions (1). The more complete description of core-valence correlation would require additional ionic states, like $2p^33s$ or $2p^33d$, to describe important $2p$–$3s$ and $2p$–$3d$ promotions. This, however, will considerably increase the target expansions, rendering the subsequent extensive scattering calculations with pseudostates unfeasible.

The BSR approach has the advantage that it allows us to generate the whole spectrum with the same accuracy, whereas the MCHF approach is based on optimization of the individual levels. Note that expansion (1) also provides us the continuum pseudostates that are used to describe the ionization processes. The number of pseudostates strongly depends on the box size. In order to cover the maximum possible target continuum we chose the small box radius of $25a_0$. On the other hand, it

TABLE I. Binding energies (in eV) for the spectroscopic target states of oxygen. Given are energy splitting listed by NIST [25] and the differences between the experiment and present calculation. Also shown are the ionization thresholds for O II. Index indicates the position of the state in the present close-coupling expansion.

Index	State	Term	NIST	Present	Difference
1	$2s^22p^4$	^3P	−13.608	−13.597	0.011
2	$2s^22p^4$	^1D	−11.651	−11.680	−0.029
3	$2s^22p^4$	^1S	−9.428	−9.421	0.007
4	$2s^22p^3(^4S)3s$	$^5S^o$	−4.472	−4.349	0.123
5	$2s^22p^3(^4S)3s$	$^3S^o$	−4.097	−3.989	0.108
6	$2s^22p^3(^4S)3p$	^5P	−2.878	−2.829	0.049
7	$2s^22p^3(^4S)3p$	^3P	−2.629	−2.572	0.057
8	$2s^22p^3(^4S)4s$	$^5S^o$	−1.780	−1.680	0.100
9	$2s^22p^3(^4S)4s$	$^3S^o$	−1.688	−1.562	0.126
10	$2s^22p^3(^4S)3d$	$^5D^o$	−1.539	−1.488	0.051
11	$2s^22p^3(^4S)3d$	$^3D^o$	−1.531	−1.478	0.053
14	$2s^22p^3(^2D)3s$	$^3D^o$	−1.078	−0.944	0.134
15	$2s^22p^3(^2D)3s$	$^1D^o$	−0.890	−0.763	0.127
	$2s^22p^3$	$^4S^o$	0.000	0.000	0.000
22	$2s^22p^3(^2D)3p$	^1P	0.418	0.464	0.046
23	$2s^22p^3(^2D)3p$	^3D	0.429	0.482	0.053
24	$2s^22p^3(^2D)3p$	^3F	0.481	0.532	0.051
25	$2s^22p^3(^2D)3p$	^1F	0.516	0.564	0.048
26	$2s^22p^3(^2D)3p$	^3P		0.591	
27	$2s^22p^3(^2P)3s$	$^3P^o$	0.506	0.651	0.145
29	$2s^22p^3(^2P)3s$	$^1P^o$	0.754	0.887	0.133
30	$2s^22p^3(^2D)3p$	^1D	0.842	0.889	0.047
34	$2s^22p^3(^2D)4s$	$^3D^o$	1.561	1.659	0.098
35	$2s^22p^3(^2P)3d$	$^3P^o$	1.673	1.697	0.024
36	$2s^22p^3(^2D)4s$	$^1D^o$	1.607	1.718	0.111
38	$2s^22p^3(^2D)3d$	$^3D^o$	1.788	1.823	0.035
39	$2s^22p^3(^2D)3d$	$^3F^o$	1.783	1.825	0.042
40	$2s^22p^3(^2D)3d$	$^1S^o$	1.786	1.826	0.040
41	$2s^22p^3(^2D)3d$	$^3G^o$	1.786	1.829	0.043
42	$2s^22p^3(^2D)3d$	$^1G^o$	1.788	1.829	0.041
43	$2s^22p^3(^2D)3d$	$^1P^o$	1.790	1.833	0.043
44	$2s^22p^3(^2D)3d$	$^1D^o$	1.796	1.838	0.042
45	$2s^22p^3(^2D)3d$	$^3S^o$	1.798	1.839	0.041
46	$2s^22p^3(^2D)3d$	$^1F^o$	1.797	1.840	0.043
48	$2s2p^5$	$^3P^o$	2.042	2.084	0.042
50	$2s^22p^3(^2P)3p$	^3S		2.157	
54	$2s^22p^3(^2P)3p$	^3D	2.163	2.278	0.115
56	$2s^22p^3(^2P)3p$	^1D	2.326	2.340	0.014
57	$2s^22p^3(^2P)3p$	^1P	2.211	2.359	0.148
58	$2s^22p^3(^2P)3p$	^3P		2.362	
61	$2s^22p^3(^2P)3p$	^1S	2.617	2.675	0.058
81	$2s^22p^3(^2P)4s$	$^3P^o$		3.410	
82	$2s^22p^3(^2P)4s$	$^1P^o$	3.288	3.411	0.123
	$2s^22p^3$	^2D	3.325		
86	$2s^22p^3(^2P)3d$	$^3F^o$		3.532	
87	$2s^22p^3(^2P)3d$	$^1F^o$		3.537	
88	$2s^22p^3(^2P)3d$	$^3P^o$	3.485	3.539	0.054
89	$2s^22p^3(^2P)3d$	$^1D^o$	3.483	3.541	0.058
90	$2s^22p^3(^2P)3d$	$^3D^o$	3.487	3.542	0.055
91	$2s^22p^3(^2P)3d$	$^1P^o$	3.490	3.544	0.054
	$2s^22p^3$	^2P	5.018		
196	$2s2p^5$	$^1P^o$		9.322	

TABLE II. Oscillator strengths of some dipole-allowed transitions from the ground and metastable states in atomic oxygen.

Lower level	Upper level	f_L	f_V	NIST
$2p^4\,{}^3P$	$2p^3({}^4S)3s\,{}^3S^o$	0.051	0.054	0.052
	$2p^3({}^4S)4s\,{}^3S^o$	0.0087	0.0093	0.0092
	$2p^3({}^4S)3d\,{}^3D^o$	0.022	0.020	0.020
	$2p^3({}^2D)3s\,{}^3D^o$	0.056	0.058	0.056
	$2p^3({}^2P)3s\,{}^3P^o$	0.083	0.090	0.079
	$2p^3({}^2D)4s\,{}^3D^o$	0.011	0.011	0.010
	$2s2p^5\,{}^3P^o$	0.066	0.071	0.062
$2p^4\,{}^1D$	$2p^3({}^2D)3s\,{}^1D^o$	0.105	0.108	0.108
	$2p^3({}^2P)3s\,{}^1P^o$	0.046	0.049	0.046
	$2p^3({}^2D)4s\,{}^1D^o$	0.017	0.017	0.017
	$2p^3({}^2D)3d\,{}^1P^o$	0.0014	0.0012	0.0016
	$2p^3({}^2D)3d\,{}^1D^o$	0.015	0.013	0.015
	$2p^3({}^2D)3d\,{}^1F^o$	0.023	0.021	0.022
$2p^4\,{}^1S$	$2p^3({}^2P)3s\,{}^1P^o$	0.134	0.139	0.137
$2p^3({}^4S)3s\,{}^5S^o$	$2p^3({}^4S)3p\,{}^5P$	0.97	1.03	1.00
$2p^3({}^4S)3s\,{}^3S^o$	$2p^3({}^4S)3p\,{}^3P$	1.05	1.04	1.03
$2p^3({}^4S)3p\,{}^5P$	$2p^3({}^4S)4s\,{}^5S^o$	0.164	0.169	0.170
	$2p^3({}^4S)3d\,{}^5D^o$	0.93	0.92	0.95
$2p^3({}^4S)3p\,{}^3P$	$2p^3({}^4S)4s\,{}^3S^o$	0.186	0.185	0.186
	$2p^3({}^4S)3d\,{}^3D^o$	0.96	0.96	0.99
$2p^3({}^2D)3s\,{}^3D^o$	$2p^3({}^2D)3p\,{}^3D$	0.317	0.334	0.330
	$2p^3({}^2P)3p\,{}^3D$	0.0019	0.0021	0.0016
$2p^3({}^2D)3s\,{}^1D^o$	$2p^3({}^2D)3p\,{}^1P$	0.179	0.201	0.189
	$2p^3({}^2D)3p\,{}^1F$	0.457	0.446	0.479
	$2p^3({}^2D)3p\,{}^1D$	0.374	0.396	0.388

restricts the number of spectroscopic target states which can be generated in this method only to the $n = 3$ states. Table I shows only the states which we consider as accurately represented in this scheme.

The assessment of the quality of our target description can also be made by comparing the results for the oscillator strengths of various transitions with experimental values and other theoretical predictions. This comparison is given in Table II for a set of transitions from the ground and metastable states of oxygen. We have shown both length and velocity values of oscillator strengths in this table. There is an excellent agreement between the present length and velocity formulations. In most cases, we note a close agreement between our results and the recommended values from NIST compilation. We may conclude that oscillator strengths for most of these transitions are very well established within a few percent. Table II also contains the f values for the excitation of the $(2s2p^5)\,{}^3P^o$ state, which is discussed later in connection with ionization. This state lies above the ionization threshold and will quickly decay by autoionization, and its excitation will ultimately contribute to the observed ionization cross sections.

B. Scattering calculations

The close-coupling expansion in our calculations includes 1116 states of atomic oxygen, with 19 bound spectroscopic states and the remaining 1097 states representing the target continuum and core-excited autoionization states. We included all singlet, triplet, and quintet target states with total electronic angular momentum $L = 0$–3. The continuum pseudostates in the present calculations cover the energy region up to 50 eV above the ionization limit. This model is referred to as BSR-1116 below.

The close-coupling equations were solved by means of the parallelized version of the BSR approach [18]. The main feature of this method is the use of B splines as a universal basis to represent the continuum wave functions in the inner region with $r \leqslant a$. The R-matrix expansion in the inner region has the form

$$\Psi_k(x_1,\dots,x_{N+1}) = \mathcal{A}\sum_{ij}\bar{\Phi}_i(x_1,\dots,x_N;\hat{\mathbf{r}}_{N+1}\sigma_{N+1})\,r_{N+1}^{-1}\,B_j(r_{N+1})\,a_{ijk} + \sum_i \chi_i(x_1,\dots,x_{N+1})\,b_{ik}. \qquad (2)$$

The channel functions $\bar{\Phi}_i$ have been constructed from the N-electron target states and the angular and spin coordinates of the incident electron. The B splines $B_j(r)$ represent the radial part of continuum functions. The additional $(N+1)$-electron bound states χ_i have been included in the second summation of the expansion. In the standard R-matrix calculations [26], the second summation is included to ensure the completeness of the total trial wave function and to compensate for orthogonality constraints imposed on the continuum functions. In the BSR approach, we use nonorthogonal one-electron radial functions and thus we do not need any additional configurations in the second summation to compensate for orthogonality constraints. In the present calculations, the bound channels χ_i were only used for a more accurate description of the $2s^22p^5$ and $2s2p^6$ negative-ion states.

The B-spline grid has the maximum interval of $0.65a_0$ in the present calculation. The chosen grid allowed us to cover electron-scattering energies up to 200 eV. There are up to 2406 scattering channels in the BSR-1116 collision model. These scattering channels give rise to generalized eigenvalue problems with matrix dimensions up to 150 000 in the B-spline basis. We calculated partial waves for total orbital angular momenta $L \leqslant 25$ in the BSR approach, taking into account the total spin and parity. It leads to a total of 156 partial waves overall. A top-up procedure based on the geometric-series approximation was used to estimate the contribution from higher L values. The parallelized version of the STGF computer code [27] has been used in the external region to calculate scattering parameters.

III. RESULTS

A. Elastic and momentum-transfer cross sections

The present angle-integrated cross sections for elastic electron scattering from oxygen atoms in the $(2p^4)\,{}^3P$ ground state together with available experimental data and theoretical calculations are displayed in Fig. 1. The only experimental data are the measurements of Williams and Allen [29]. They measured absolute angle-differential elastic scattering cross sections at five incident electron energies, corresponding to incident electron wave numbers of $k = 0.2a_0^{-1}$, $0.4a_0^{-1}$,

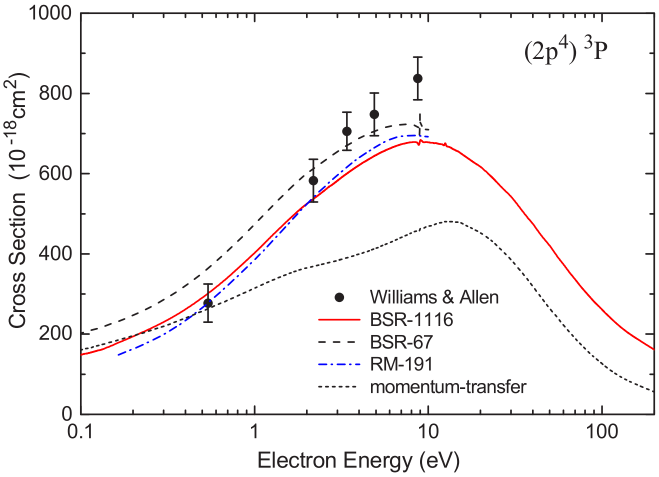

FIG. 1. Angle-integrated cross sections for elastic electron scattering from oxygen atoms in their $(2p^4)\,^3P$ ground state. The present BSR-1116 results are compared with the BSR-67 calculation [28], with the calculation of Plummer *et al.* [12] (RM-191), and with the experimental data of Williams and Allen [29]. The momentum-transfer cross sections are also shown.

$0.5a_0^{-1}$, $0.6a_0^{-1}$, and $0.8a_0^{-1}$. They also presented separately measured total cross sections at the first four energies, as well as elastic cross sections for all five energies obtained from their differential scattering data via a phase-shift analysis.

From the available calculations, we choose for comparison our previous BSR calculation [28] and the 191-state trial calculation of Plummer *et al.* [12]. Our previous study included careful analysis of convergence of the close-coupling expansion by considering different models including from first 3 to 67 target states. The elastic cross sections at low energies were found to show a decreasing trend with increase in the size of the close-coupling expansion. The most extended BSR-67 model was intended to account for the polarization of the ground state as much as possible. The available computational resources did not allow to include all continuum pseudostates, and in the BSR-67 model we, therefore, selectively included only those states which give the principal contribution to the polarizability of the target. The present BSR-1116 model includes many more pseudostates and as seen from Fig. 1 it results in further reduction of cross sections from 10% to 20%. Our present results are in very close agreement with the trial calculation of Plummer *et al.* [12] that included 191 target states in the close-coupling expansion. We may consider the elastic cross sections as fully converged. Note also that the polarizability of the ground state in the present calculation is 4.87 a.u., which closely agrees with the calculated value of 4.89 a.u. from the *R*-matrix calculation of Plummer *et al.* [12] and with the experimental value of 5.2 ± 0.4 a.u. [30]. The remaining discrepancies with the measurements of Williams and Allen [29] can be referred to their phase-shift analysis, which require additional more careful consideration of their differential cross sections.

The elastic cross sections for electron scattering from the metastable $(2p^4)\,^1D$ and $(2p^4)\,^1S$ states of oxygen are presented in Figs. 2 and 3, respectively. In order to illustrate the influence of the target continuum, we compare the present results from the BSR-1116 model with our previous BSR-26 calculation [8], where the close-coupling expansion contains only the bound and autoionizing states of oxygen. Inclusion of continuum pseudostates in the BSR-1116 model decreases considerably the $(2p^4)\,^1D$ cross sections in the near-threshold energy region. The opposite effect is for elastic scattering from the $(2p^4)\,^1S$ state where the BSR-26 cross sections are considerably lower than the BSR-1116 results in the wide energy region from the threshold to 50 eV. The $(2p^4)\,^1D$ and $(2p^4)\,^1S$ cross sections also show prominent structure around 17 eV, which is due to the $(2s2p^6)\,^1S$ resonance.

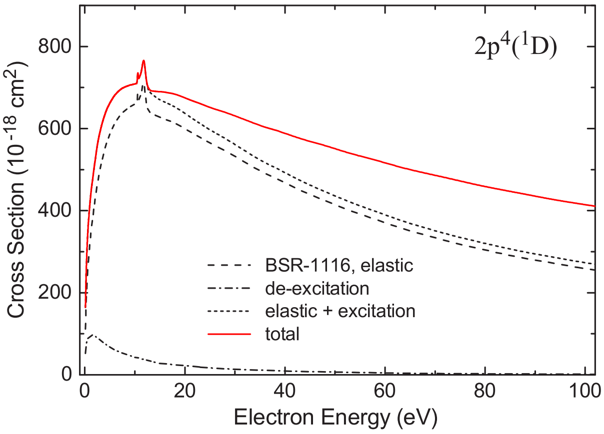

FIG. 2. Angle-integrated cross sections for elastic electron scattering from oxygen atoms in the metastable $(2p^4)\,^1D$ states. The current BSR-1116 results are compared with those from a BSR-26 model [8]. The momentum-transfer cross sections are also shown.

Momentum-transfer cross sections shown in Figs. 1–3 are all well below the corresponding elastic cross sections. The only exception is the narrow near-threshold region, where the momentum-transfer cross sections are very close to the elastic cross sections. Clearly, the momentum-transfer cross sections should be used in the plasma modeling applications.

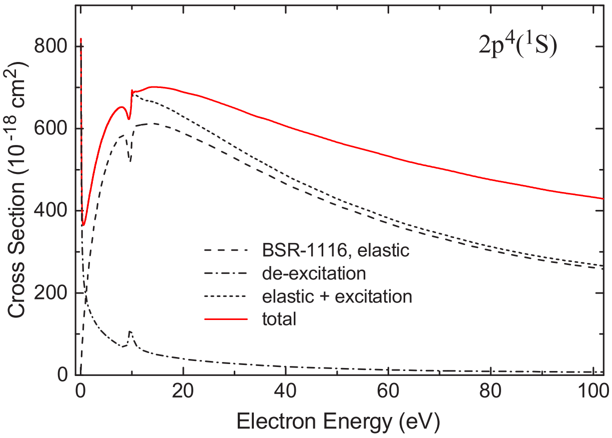

FIG. 3. Angle-integrated cross sections for elastic electron scattering from oxygen atoms in the metastable $(2p^4)\,^1S$ states. The current BSR-1116 results are compared with those from a BSR-26 model [8]. The momentum-transfer cross sections are also given.

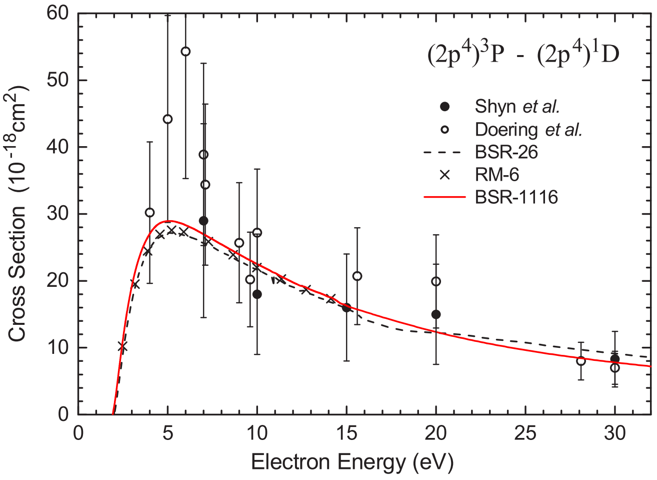

FIG. 4. The excitation cross sections for the forbidden $(2p^4)\,^3P$–$(2p^4)\,^1D$ transition. The present BSR-1116 results are compared with those from a BSR-26 model [8] and a six-state R matrix with polarized pseudostates (RM-6) [12]. Also shown are experimental data of Shyn *et al.* [31] and Doering [32].

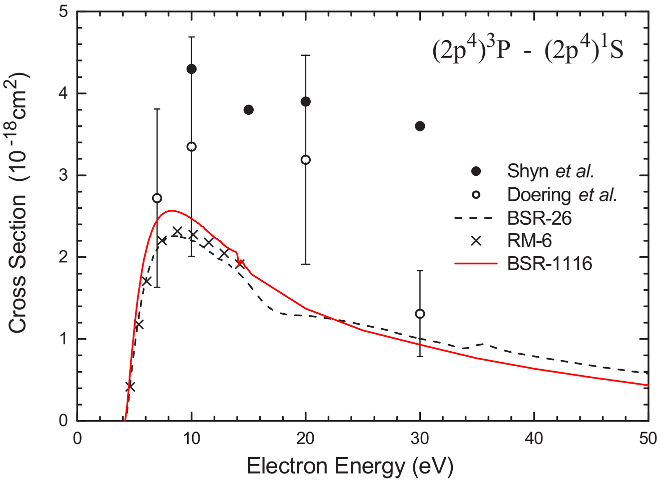

FIG. 5. The excitation cross sections for the forbidden $(2p^4)\,^3P$–$(2p^4)\,^1S$ transition. The present BSR-1116 results are compared with those from a BSR-26 model [8] and a six-state R matrix with polarized pseudostates (RM-6) [12]. Also shown are experimental data of Shyn *et al.* [31] and Doering and Gulcicek [33].

B. Excitation cross sections

1. *Excitation of the forbidden transitions within the ground configuration*

Figure 4 compares our excitation cross sections for the $(2p^4)\,^3P$–$(2p^4)\,^1D$ (630.0 nm) transition obtained in the 1116-state model with the previous BSR [8] and R-matrix calculations [12], and with the experimental results [31,32]. All theoretical calculations agree very well with each other at all electron energies. It confirms our previous conclusion [8] that for this exchange forbidden transition the channel-coupling effects are not important and the cross sections can be considered as fully converged. Theoretical data also agree with measured values within the experimental error bars, but at lower energies there are differences between various results. The measurement of Doering [32] exhibits a sharp peak around 6 eV, whereas all calculations predict a much lower broad peak around 5 eV. Further measurements are required to resolve this discrepancy. Note that the present calculation seems to contain all physical effects that are important for low-energy electron scattering. The cross sections do not appear to depend noticeably on the accuracy of target wave functions [8].

The energy behavior of the cross sections for the $(2p^4)\,^3P$–$(2p^4)\,^1S$ transition shown in Fig. 5 is very similar to that of the $(2p^4)\,^3P$–$(2p^4)\,^1D$ transition discussed above. However, the forbidden ^3P-^1S transition is much weaker, and the cross sections for these two transitions differ by about an order of magnitude at a given electron energy. Again, all theoretical predictions shown in the figure agree very well with each other; however, the agreement with the available measurements is clearly not satisfactory. In spite of 50% uncertainty in the measured data of Shyn and Sharp [31], their results are much higher than all theoretical calculations and lie completely outside of theoretical predictions. The measurements of Doering and Gulcicek [33] agree better with calculations, but still differ considerably at intermediate energies. These measurements also have large uncertainties (35%) to make any final conclusion. Clearly an experiment with smaller uncertainties in data is needed.

The cross sections for the $(2p^4)\,^1D$–$(2p^4)\,^1S$ transition are shown in Fig. 6 as a function of electron energy. No experimental data exist for this transition. We compare only the most recent calculations, and they all reasonably agree with each other, though as discussed in the paper of Zatsarinny and Tayal [8], there are significant discrepancies with earlier calculations. The differences in magnitude of cross sections from various calculations can be attributed to the differences in the target description. We also found that convergence of the partial wave expansion for this transition is slow, and higher partial wave contributions need to be evaluated to obtain converged cross sections. The distinctive feature of the cross section for the ^1D-^1S transition is a large resonance at low

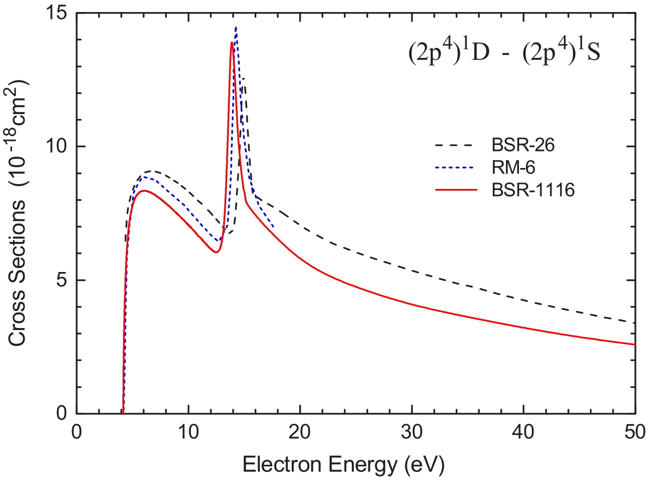

FIG. 6. The excitation cross sections for the forbidden $(2p^4)\,^1D$–$(2p^4)\,^1S$ transition. The present BSR-1116 results are compared with those from a BSR-26 model [8] and a six-state R matrix with polarized pseudostates (RM-6) [12].

electron energies. This resonance is due to the $\mathrm{O}^-(2s2p^6)\,^2S$ state with energy $E_r = 13.877$ eV and width $\Gamma_r = 970$ meV. The large width is due to very large matrix elements for the interaction of the quasibound $(2s2p^6)\,^2S$ state with the $2s2p4kd$ continuum, i.e., a $2p^2$–$2skd$ dipole interaction. Our width is much smaller than predicted in earlier calculations (see a full discussion in the review by Buckman and Clark [34]). The experiment should be able to detect this strong resonance either in photodetachment measurements or in an electron-scattering experiment. Such an experiment is highly desirable to confirm the theoretical predictions.

2. *Excitation of the 3s $^3S^o$, 3s′ $^3D^o$, and 3s″ $^3P^o$ states*

The excitation of the $3s\,^3S^o$ level in the oxygen atom results in the ultraviolet emission at 130.4 nm. This line is among the dominant features in spectra of Earth's atmosphere as well as atmospheres of other planets such as Mars and Venus. For this reason, cross sections for electron-impact excitation of the $3s\,^3S^o$ state had attracted much attention from both theory and experiment. A set of measurements was carried out by Doering and co-workers [35–38] with increasing improvements in apparatus and normalization standards. The cross sections were determined at several energies from 13.4 to 100 eV. The excitation function, however, displayed some scatter among the accumulated data, especially at low energies. It was for this reason that Doering and Yang [39] reanalyzed the data and provided a "best guess" curve based on the fit of a Bethe line to the data. This procedure, however, is not justified in the low-energy region.

More recently, new measurements for the $3s\,^3S^o$ excitation function were reported by Kanik *et al.* [40] at electron energies of 30, 50, and 100 eV and by Johnson *et al.* [41] at lower energies down to 15 eV. The combined data from these measurements provide a smooth excitation function over whole energy range. Comparing with previous results of Doering and Yang, two data sets agree very well at 30 eV and higher energies, but new cross sections are consistently lower in magnitude at low energies. All relevant data were examined one more time by Johnson *et al.* [7] in order to provide recommended cross sections suitable for different applications. When reviewing these data, some data points have been superseded by successive measurements and reanalysis, and some data were considered outside the trend supported by the remaining data and theory. These data points were considered anomalous and thus were omitted from consideration in making the final recommendation. The resulting recommended $(2p^4)\,^3P$–$(2p^33s)\,^3S^o$ cross section alongside those experimental data points included into consideration are shown in Fig. 7.

For comparison with other theories, we choose the most recent and most extensive calculations. The BSR-26 calculation by Zatsarinny and Tayal [8] includes only bound states and the cross sections are well above the experimental values at all energies up to 100 eV. In their analysis they also checked a set of other models with different numbers of target states in the close-coupling expansion and concluded that the theoretical cross sections seem to be converged with respect to the coupling to bound states. Though the cross sections may still be uncertain due to the neglect of coupling to the continuum, it was difficult to anticipate a large reduction in the theoretical cross section at 100 eV. They suggested that there are problems with the normalization of the measured cross-section data. Note that the cross sections at higher energies are proportional to the oscillator strengths, and the calculations discussed here are all in very close agreement with experimental values for the oscillator strength (see Table II).

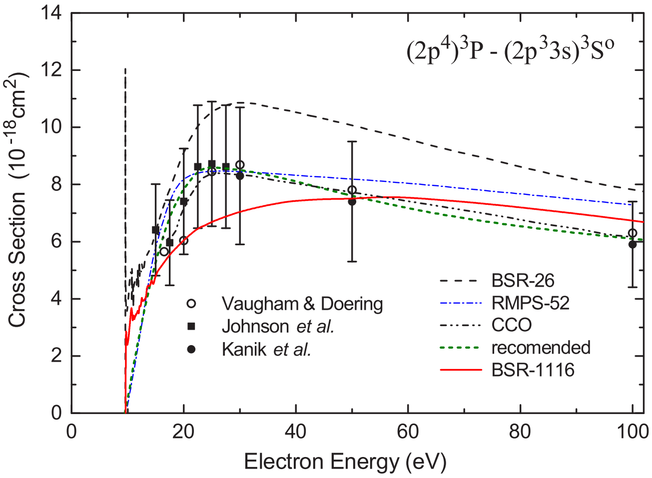

FIG. 7. The excitation cross sections for the allowed $(2p^4)\,^3P$–$(2p^33s)\,^3S^o$ transition. The present BSR-1116 results are compared with those from a BSR-26 model [8], a 52-state RMPS calculation (RMPS-52) [11], a CCO calculation of Wang and Zhou [42], and experimental data of Vaughan and Doering [37], Kanik *et al.* [40], and Johnson *et al.* [41]. The recommended cross sections from Johnson *et al.* [7] are also shown.

Figure 7 also shows more recent RMPS [11] and momentum-space coupled-channels-optical (CCO) [42] calculations which partly include the influence of the target continuum. These calculations show a big reduction of cross sections at intermediate energies and the results agree closely with experimental data. Our present BSR-1116 model provides an even bigger reduction of the cross sections in the region of the maximum around 20 eV. At first sight, the present calculations seem to disagree with experiment; however, all calculations are still within the experimental error bars. The final conclusion about the accuracy of the cross sections for the $(2p^4)\,^3P$–$(2p^33s)\,^3S^o$ transition requires more accurate experimental data. Note also that the cross sections from the different calculations have different energy dependence at higher energies. Partly, it may be concerned with the different representation of target wave functions. The target description in the BSR-26 and BSR-1116 models is very close, so the differences between these two calculations directly show the influence of the target continuum.

The excitation cross sections for the $(2p^4)\,^3P$–$(2p^33s')\,^3D^o$ transition are compared in Fig. 8. They exhibit the similar trend in dependence on the size of the close-coupling expansions as discussed above for the $3s\,^3P^o$ state. The BSR-26 model clearly overestimates the cross sections for a wide range of energies and the inclusion of continuum pseudostates in the RMPS calculation of Tayal [11] reduces the cross sections by 15–25 %, bringing them in closer agreement with experimental data. Full inclusion of the target continuum in the BSR-1126

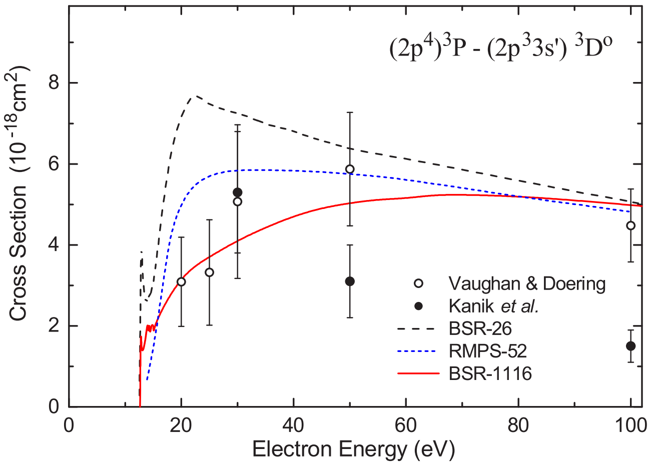

FIG. 8. The excitation cross sections for the allowed $(2p^4)\,^3P$–$(2p^33s')\,^3D^o$ transition. The present BSR-1116 results are compared with those from a BSR-26 model [8], a 52-state RMPS calculation (RMPS-52) [11], and experimental data of Vaughan and Doering [37] and Kanik *et al.* [40].

model further reduces the cross sections, which now are in much closer agreement with the measurements of Vaughan and Doering [43]. It can be considered a confirmation of the large influence of the target continuum in the case of atomic oxygen and its appropriate representation in the BSR-1116 model. The experimental cross sections of Kanik *et al.* [40], especially at electron energies of 50 and 100 eV, considerably differ in magnitude from other results and may be considered as having some normalization-type error.

The large differences between BSR-26 and BSR-1116 models due to the target continuum are also found for the $(2p^4)\,^3P$–$(2p^33s'')\,^3P^o$ transition shown in Fig. 9. Inclusion of the target continuum leads to the 30% reduction at intermediate energies of 30–50 eV. The BSR-1116 cross sections agree closely with the experimental data at all electron energies, except for 50 eV from the measurements of Vaughan and Doering [43]. This value is clearly out of the smooth energy dependence expected in this energy region and can be considered erroneous.

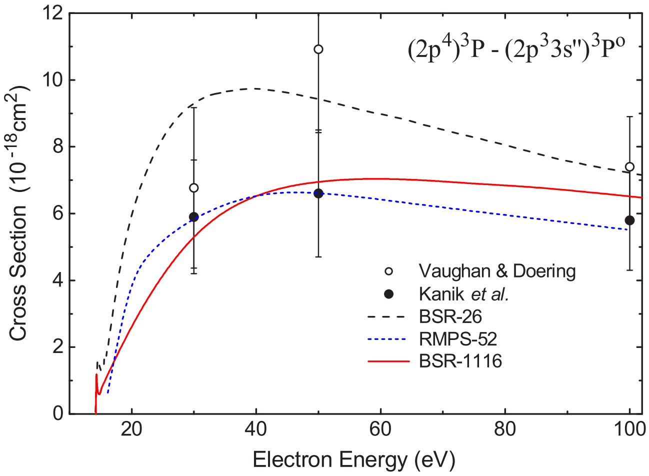

FIG. 9. The excitation cross sections for the allowed $(2p^4)\,^3P$–$(2p^33s'')\,^3P^o$ transition. The present BSR-1116 results are compared with those from a BSR-26 model [8], a 52-state RMPS calculation (RMPS-52) [11], and experimental data of Vaughan and Doering [43] and Kanik *et al.* [40].

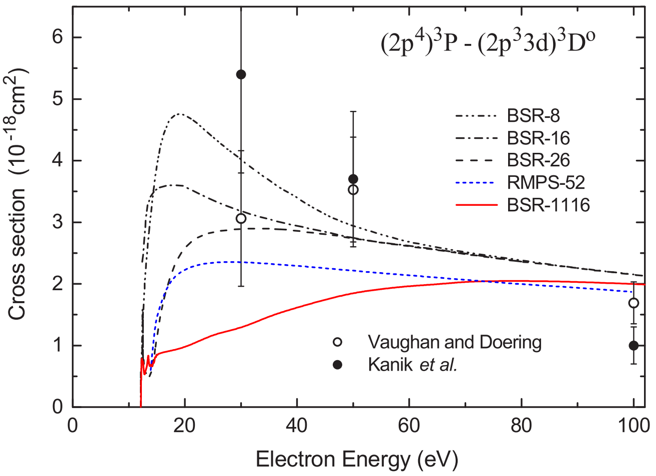

FIG. 10. The excitation cross sections for the allowed $(2p^4)\,^3P$–$(2p^33d)\,^3D^o$ transition. The present BSR-1116 results are compared with those from the BSR-8, BSR-16, and BSR-26 models [8], the 52-state RMPS calculations (RMPS-52) [11], and experimental data of Vaughan and Doering [43] and Kanik *et al.* [40].

3. Excitation of the $(2p^4)\,^3P$–$(2p^33d)\,^3D^o$ *transition*

The excitation cross sections for the $(2p^4)\,^3P$–$(2p^33d)\,^3D^o$ transition shown in Fig. 10 were found to be extremely sensitive to the coupling to higher excited states and target continuum. In order to illustrate this, we compare a set of models with different numbers of target states included in the close-coupling expansions. In the BSR-8 model where $3d\,^3D^o$ is the highest target state, the cross section has a broad near-threshold maximum. This maximum diminishes with increasing number of target states and almost disappears in the BSR-26 model with all target states to be the bound states. The target continuum is found to have even more influence on cross sections for this transition. Its inclusion leads to substantial change in the energy dependence of cross sections, and our BSR-1116 calculations predict that cross sections gradually increase with energy up to 100 eV, where they converges to other models. The RMPS calculation of Tayal [11] confirms this behavior; the differences with the present calculations can be explained as due to the use of different atomic wave functions to describe this state. The extreme sensitivity of the $2p$-$3d$ excitation also was found for other atoms, for example, in the electron scattering from neon atoms, and was also confirmed in other calculations [16,44].

The present BSR-1116 cross sections for the $(2p^4)\,^3P$–$(2p^33d)\,^3D^o$ transition differ considerably from the available experimental data of Vaughan and Doering [43] and Kanik *et al.* [40]. The experimental data also differ considerably from each other. At 30 eV, for example, the measurements differ by a factor of 2 with each other, and the present cross sections are lower from the experimental values of Vaughan and Doering [43] and Kanik *et al.* [40] by factors of 2.5 and 5, respectively. At 50 eV, the measured values

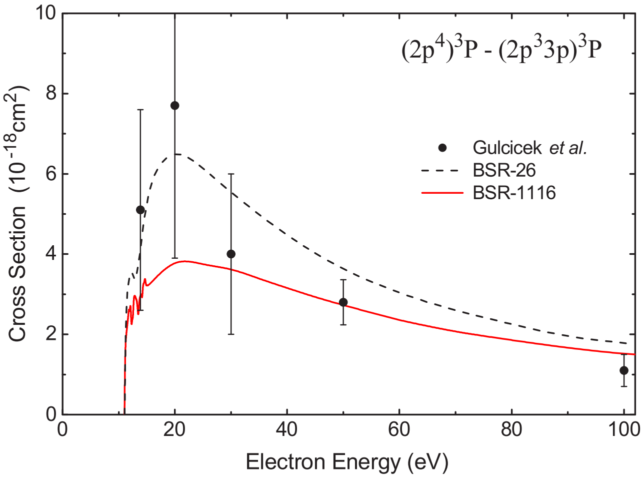

FIG. 11. The excitation cross sections for the $(2p^4)\,^3P$–$(2p^33p)\,^3P$ transition as a function of electron energy. The present BSR-1116 results are compared with those from a BSR-26 model [8] and experimental data of Gulcicek *et al.* [45].

closely agree with each other; however, they again exceed the BSR-1116 results by a factor of 2. Only at 100 eV did we obtain reasonable agreement with the measured value of Vaughan and Doering [43], but the value of Kanik *et al.* [40] is still two times smaller than the present calculated result. Note that at 100 eV all calculations provide very close results, showing the channel-coupling effects quickly diminish with electron energy.

4. *Excitation of the* $(2p^33p)\,^3P$ *and* $(2s2p^5)\,^3P^o$ *states*

Figure 11 compares the excitation cross sections for the quadrupole $(2p^4)\,^3P$–$(2p^33p)\,^3P$ transition. As in the case of the dipole transitions discussed above, the channel-coupling effects are also important for this transition, and inclusion of the target continuum reduces the cross sections almost twice in the near-threshold maximum-energy region in comparison to the BSR-26 model. At higher energies, the cross sections from different approximate models converge to each other. We note a large influence of target representation in this case due to strong term dependence of the outer $3p$ orbital. Agreement with the experimental data of Gulcicek *et al.* [45] is scattered. Good agreement with the BSR-1116 is seen for the higher energies at 30, 50, and 100 eV, whereas the experimental data overestimate the cross sections at lower energies of 15 and 20 eV.

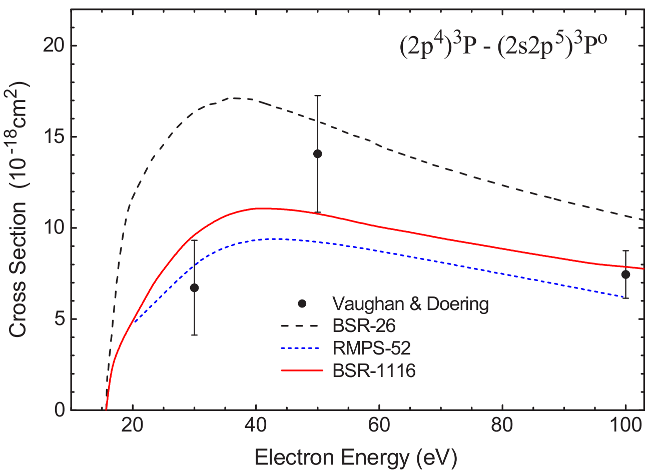

FIG. 12. The excitation cross sections for the $(2p^4)\,^3P$–$(2s2p^5)\,^3P^o$ transition as a function of electron energy. The present BSR-1116 results are compared with those from a BSR-26 model [8], a 52-state RMPS calculation (RMPS-52) [11], and experimental data of Vaughan and Doering [43].

The excitation cross sections for the $(2p^4)\,^3P$–$(2s2p^5)\,^3P^o$ transition are shown in Fig. 12. We see large differences between the BSR-26 and BSR-1116 models. There are two possible explanation for these differences. First, the $(2s2p^5)\,^3P^o$ state shows strong configuration mixing with other configurations, and its representation in different models may differ considerably. As a result, the present oscillator strength of 0.66 for this transition differs substantially from the oscillator strength of 0.92 in the BSR-26 model [8]. It may lead to 30% reduction of cross sections at higher energies. Second, further reduction of cross sections at lower energies may be due to a much more accurate description of channel-coupling effects in the BSR-1116 model. Overall, the inclusion of the target continuum in the BSR-1116 model leads to better agreement with experiment.

5. *Excitation of the* $(2p^33s)\,^5S^o$ *and* $(2p^33p)\,^5P$ *states*

Examples of the exchange transitions from the ground state are given in Figs. 13 and 14 for excitation of the $(2p^33s)\,^5S^o$ and $(2p^33p)\,^5P$ states, respectively. These exchange transitions have a characteristic near-threshold maximum and quickly decrease with energy. Calculations also show noticeable resonance structure in the near-threshold region. The BSR-26 and BSR-1116 models differ considerably at intermediate energies, indicating the strong influence of coupling to higher excited states and the target continuum. Especially it is true for excitation of the $(2p^33p)\,^5P$ state where the maximum cross section around 20 eV reduces three times and now disagrees

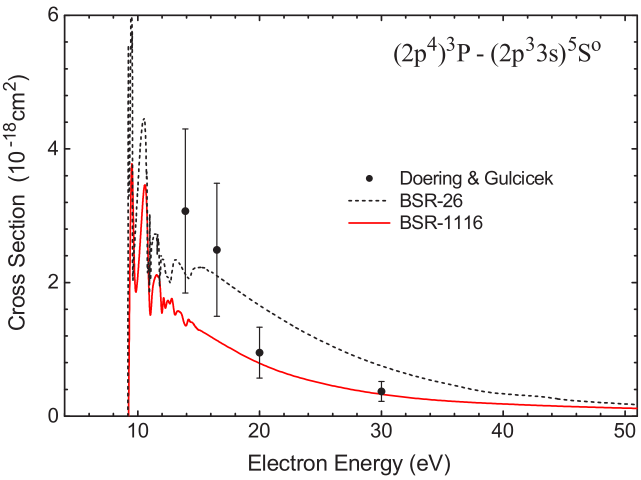

FIG. 13. The $(2p^4)\,^3P$–$(2p^33s)\,^5S^o$ excitation cross sections as a function of electron energy. The present BSR-1116 results are compared with those from a BSR-26 model [8] and experimental data of Doering and Gulcicek [46].

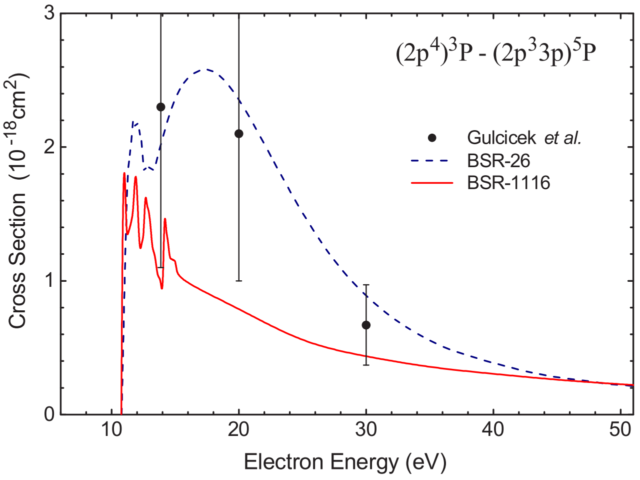

FIG. 14. The excitation cross sections for the $(2p^4)\,^3P$–$(2p^33p)\,^5P$ transition as a function of electron energy. The present BSR-1116 results are compared with those from a BSR-26 model [8] and experimental data of Gulcicek *et al.* [45].

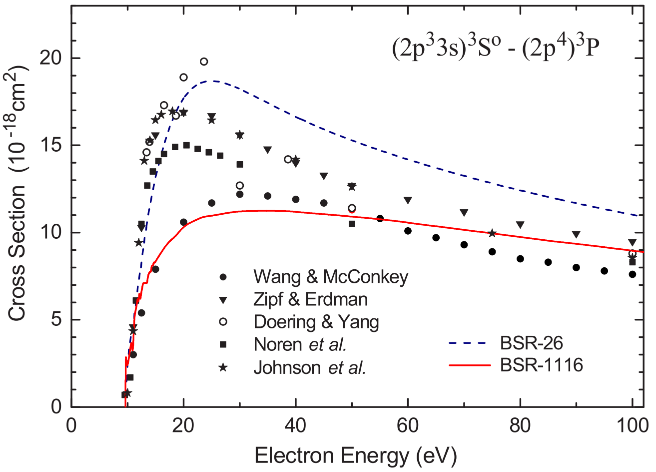

FIG. 15. The $(2p^33s)\,^3S^o$–$(2p^4)\,^3P$ emission cross sections as a function of electron energy. The present BSR-1116 results are compared with those from a BSR-26 model [8] and experimental data of Wang and McCokey [49], Zipf and Erdman [48], Doering and Yang [39], Noren *et al.* [50], and Johnson *et al.* [47].

with the experiment of Gulcicek *et al.* [45]; however, the experimental error bars in this case are too large to make a final conclusion. Note that, as was found in Ref. [8], the coupling to autoionizing states plays a crucial role for the $(2p^4)\,^3P$–$(2p^33p)\,^5P$ transition, and this coupling is much better described in the BSR-1116 model. For the $(2p^33s)\,^5S^o$ state, inclusion of the target continuum improves the agreement with the experiment of Doering and Gulcicek [46] at higher energies of 20 and 30 eV; however, at lower energies the calculations are considerably lower than the experimental values.

6. Optical emission cross sections

Emissions from atomic oxygen induced by electron impact are important features in different astrophysical sources. For this reason, accurate emission cross sections are needed for modeling and diagnostic analyses of the oxygen-bearing atmospheric and nebular environments. They are perhaps the most applicable electron-impact parameters used in astrophysical modeling calculations. The excitation cross sections, considered above, provide probabilities for the direct excitation of an atomic state from the ground and excited states, while the emission cross sections provide the accumulated excitation of an atomic level through both direct excitation and cascade from higher-lying levels. The consistent calculation of the emission cross sections requires consideration of a large number of levels simultaneously, in the framework of the same model.

Electron-impact-induced emission cross sections of atomic oxygen have been widely investigated in the past. The existing data have been reviewed by Johnson *et al.* [47], with the final conclusion that the current status of atomic-oxygen emission cross sections requires further experimental study due to the continued lack of agreement among the available data, especially in the peak energy region of the cross sections. Discrepancies also remain among the available theoretical emission cross sections. Below we discuss the four most studied transitions in the vacuum ultraviolet (VUV) wavelength region, namely, $(2p^33s)\,^3S^o$–$(2p^4)\,^3P$ (130.4 nm), $(2p^33d)\,^3D^o$–$(2p^4)\,^3P$ (102.7 nm), $(2p^33s')\,^3D^o$–$(2p^4)\,^3P$ (98.9 nm), and $(2p^33s'')\,^3D^o$–$(2p^4)\,^3P$ (87.8 nm) emissions.

The 130.4-nm-emission cross sections are shown in Fig. 15 as a function of electron energy. The earlier measurements of optical emission cross sections for this emission line were made by Zipf and Erdman [48] and Wang and McConkey [49]. The absolute values of emission cross sections by Wang and McConkey [49] were much smaller than the measurement of Zipf and Erdman [48] for a wide range of incident electron energies. To resolve these discrepancies, Doering and Yang [39] and Noren *et al.* [50] carried out new measurements. While Noren *et al.* performed a direct optical emission experiment, Doering and Yang determined emission cross sections by summing the direct excitation cross sections for the $3s\,^3S^o$ level and its main cascade contribution from the $3p\,^3P$ level. Though new results agree at high energies, the discrepancies remained in the near-threshold energy region. In an attempt to settle the issue, Johnson *et al.* [47] repeated the measurements with further improvement to the apparatus and analytical procedure employed by Noren *et al.* [50]. The new measurements resulted in reducing the experimental uncertainties by 10% and a slight increase (∼13%) in the absolute magnitude of the cross sections.

Our previous calculations in the BSR-26 model agree well with the estimates of Doering and Yang at low energies below 25 eV and also with the measured data of Noren *et al.* and Zipf and Erdman at energies below 20 eV, but overestimate at higher energies. The shape of the BSR-26 emission cross section is in good agreement with the experiments of Zipf and Erdman and Noren *et al.*, but discrepancies in magnitude exist. At that time we concluded that the emission cross sections of Wang and McConckey were substantially underestimated. However, the present BSR-1116 results are considerably smaller in magnitude for a wide range of energies and they most closely agree with the emission cross sections of Wang and McConckey. The large reduction in the cross sections is due to inclusion of coupling to the target continuum as

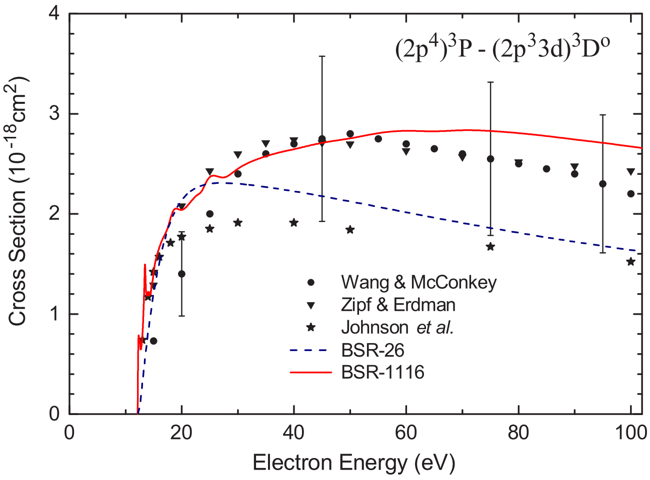

FIG. 16. The $(2p^33d)\,^3D^o$–$(2p^4)\,^3P$ emission cross sections as a function of electron energy. The present BSR-1116 results are compared with those from a BSR-26 model [8] and experimental data of Zipf and Erdman [48], Wang and McConkey [49], and Johnson *et al.* [47].

discussed above in connection with direct-excitation cross sections for the $3s\,^3S^o$ state in Fig. 7.

The emission cross sections for the $(2p^33d)\,^3D^o$–$(2p^4)\,^3P$ transition are presented in Fig. 16. The present results are compared with the experimental data of Zipf and Erdman [48], Wang and McConkey [49], and Johnson *et al.* [47]. The BSR-26 cross sections agree with experiment at low near-threshold energies, but at higher energies they significantly underestimate the measurements. The best agreement of the present BSR-1116 results is with the early measurements of Zipf and Erdman for a wide range of energies from threshold to 100 eV. The large differences between BSR-26 and BSR-1116 results are primarily due to considerable underestimation of the cascade contribution in the BSR-26 model due to more restricted close-coupling expansion. In view of the present results, the latest measurements by Johnson *et al.* seem to have error in the absolute normalization. It is worth noting that the $(2p^33d)\,^3D^o$–$(2p^4)\,^3P$ transition shows the biggest reduction of the cross sections due to the inclusion of the target continuum as discussed above, and the close agreement with the emission cross sections confirms these findings.

Similar results are found for the $(2p^33s')\,^3D^o$–$(2p^4)\,^3P$ transition shown in Fig. 17. Again, the close agreement of the present BSR-1116 results is with the early measurements of Zipf and Erdman, whereas the latest measurements by Johnson *et al.* considerably underestimate the emission cross sections. Clearly the BSR-26 model does not contain cascade contribution to a full extent.

For the $(2p^33s'')\,^3P^o$–$(2p^4)\,^3P$ emission cross sections shown in Fig. 18 we see close agreement between experimental results of Wang and McConkey [49] and Johnson *et al.* [47] and with the present BSR-1116 theory. All cross sections agree within 15% for electron energies up to 100 eV. Comparison with the direct-excitation cross sections shows that the cascade contribution in this case consists from 10% to 20%. Overall, the present BSR-1116 model considerably improves the agreement with the available measured emission cross sections.

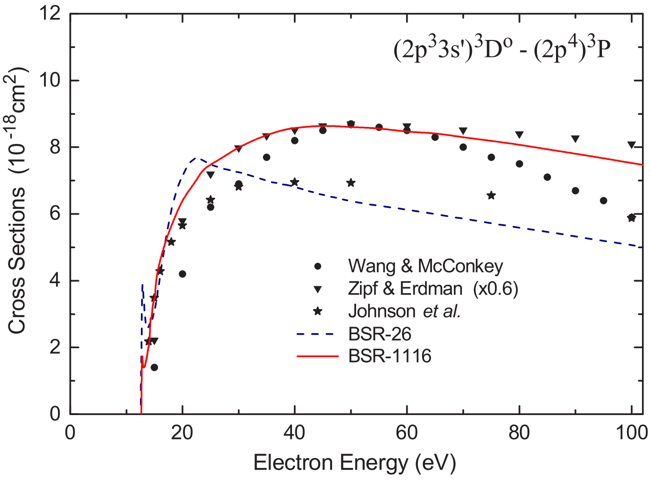

FIG. 17. The $(2p^33s')\,^3D^o$–$(2p^4)\,^3P$ emission cross sections as a function of electron energy. The present BSR-1116 results are compared with those from a BSR-26 model [8] and experimental data from Zipf and Erdman [48], Wang and McConkey [49], and Johnson *et al.* [47].

C. Ionization cross sections

The electron-impact ionization cross sections for atomic oxygen from the $(2p^4)\,^3P$ ground state are displayed in Fig. 19. The present ionization cross sections were obtained by adding the excitation cross sections for all target states above the ionic ground state including the direct contribution from the continuum pseudostates and the excitation cross sections of quasidiscrete states in the continuum. The radiation damping should play a negligible role in the present case. The latter process is usually known as excitation autoionization. The direct ionization cross sections are also displayed to

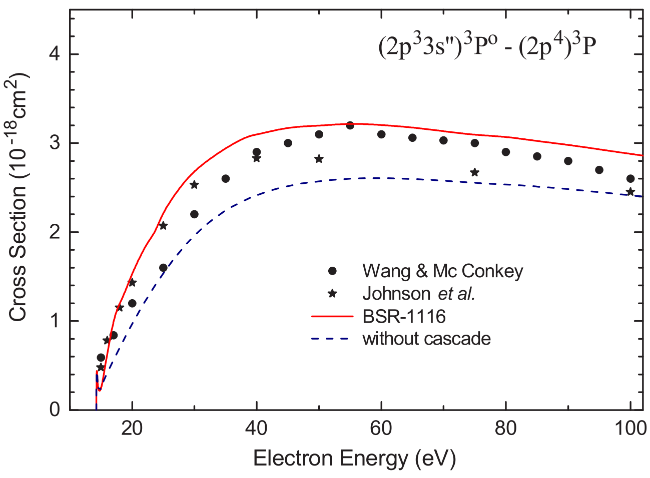

FIG. 18. The $(2p^33s'')\,^3P^o$–$(2p^4)\,^3P$ emission cross sections as a function of electron energy. The present BSR-1116 results are shown with and without cascade contributions, and compared with experimental data of Wang and McConkey [49] and Johnson *et al.* [47].

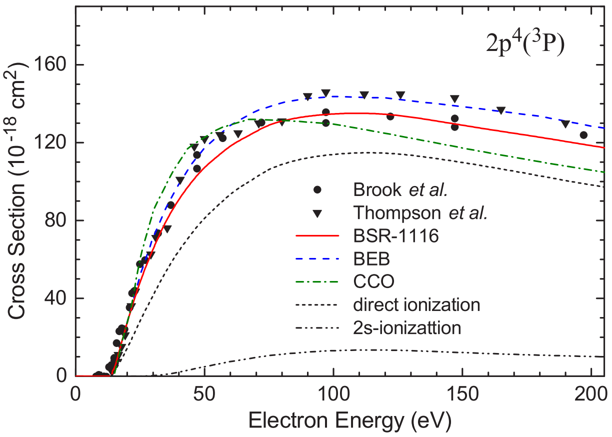

FIG. 19. Angle-integrated cross sections for electron-impact ionization of oxygen atoms in their $(2p^4)\,^3P$ ground state. The present BSR-1116 results are compared with the BEB predictions of Kim and Desclaux [53], the CCO calculations of Wang and Zhou [42], and the experimental data of Brook *et al.* [51] and Thompson *et al.* [52]. The direct ionization cross sections and the partial contribution of the $2s$ ionization are also shown.

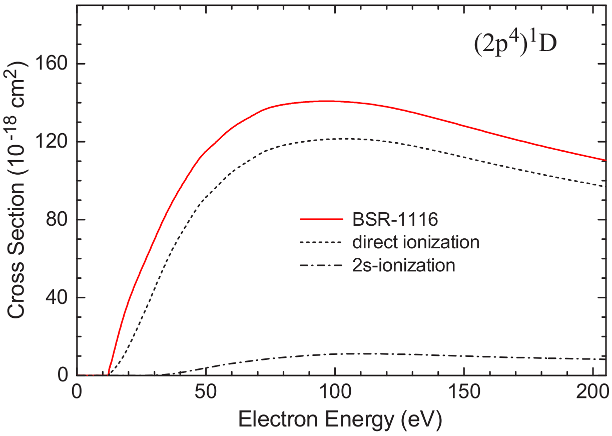

FIG. 20. Angle-integrated cross sections for electron-impact ionization of oxygen atoms in the metastable state $(2p^4)\,^1D$. The direct ionization cross sections and the partial contribution of the $2s$ ionization are also shown.

demonstrate the importance of the excitation-autoionization contribution. In oxygen, the dominant contribution to the excitation autoionization is expected from the $(2s2p^5)\,^1P^o$ and $^3P^o$ states due to the strong $2s$-$2p$ transition. The partial contribution of the $2s$ ionization is also shown. The $2s$ ionization cross sections contribute within about 15% to the ionization cross sections. It is evident from Fig. 19 that the fully *ab initio* BSR results are in overall good agreement with the experimental results of Brook *et al.* [51] for a wide range of energies from threshold to 200 eV. Thompson *et al.* [52] reported a small but distinct step near 100 eV, which is not visible in the other experimental results and in the present calculations. The present ionization cross sections have also been compared with the semiempirical binary encounter Bethe (BEB) results of Kim and Desclaux [53]. It is clear from the figure that the semiempirical BEB predictions of Kim and Desclaux [53] overestimate the BSR ionization cross sections by ~10% at maximum and could be considered in reasonable agreement with the present results. The differences could be attributed to the contribution of excitation autoionization. As seen from a comparison of direct ionization cross sections, the excitation autoionization in atomic oxygen increases the total ionization cross section by ~20% at the peak. Therefore, the major excitation-autoionization channels must be included in the calculation to obtain good agreement between theory and experiment. Figure 19 also shows recent CCO calculation of Wang and Zhou [42]. These agree with the present results in magnitude but show somewhat different shape as a function of electron energy.

The ionization cross sections from the metastable $2p^4\,^1D$ and ^1S states of oxygen are shown in Figs. 20 and 21, respectively. The electron-impact direct ionization and $2s$ ionization cross sections are also shown. These cross sections have the same order of values as the ground-state cross sections. There are no other theoretical or experimental results available for comparison in these cases. The excitation autoionization is also important, providing corrections up to 20%. For all ionization processes, the $2p$ ionization is the dominant process, whereas the $2s$ ionization contributes not more than 15%.

D. Total cross sections

Finally, the present grand total cross sections from the ground $(2p^4)\,^3P$ and metastable $(2p^4)\,^1D$ and $(2p^4)\,^1S$ states are shown in Figs. 22–24. Specifically, the grand total cross sections are comprised of the elastic contribution, all summed up inelastic excitation processes, ionization, and—in the case of the excited metastable initial states $(2p^4)\,^1D$ and $(2p^4)\,^1S$—*superelastic deexcitation* cross sections. The elastic cross sections provide the largest contribution over the energy range shown in these figures. The ionization cross sections provide substantial contribution at higher energies above 40 eV. Excitation processes represent overall less than 10% of the grand total cross sections. The set of electron collision elastic, momentum-transfer, total excitation, and ionization

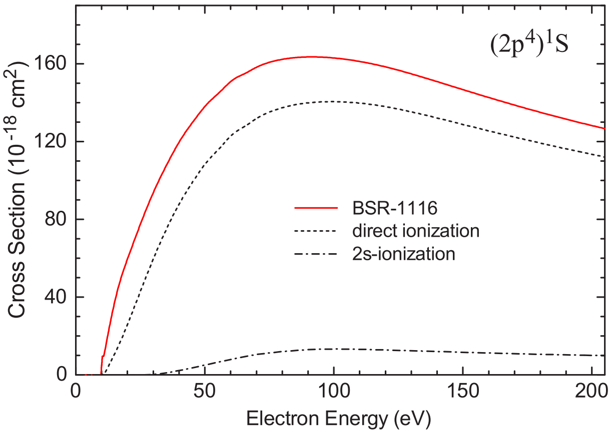

FIG. 21. Angle-integrated cross sections for electron-impact ionization of oxygen atoms in the metastable $(2p^4)\,^1S$ state. The direct ionization cross sections and the partial contribution of the $2s$ ionization are also shown.

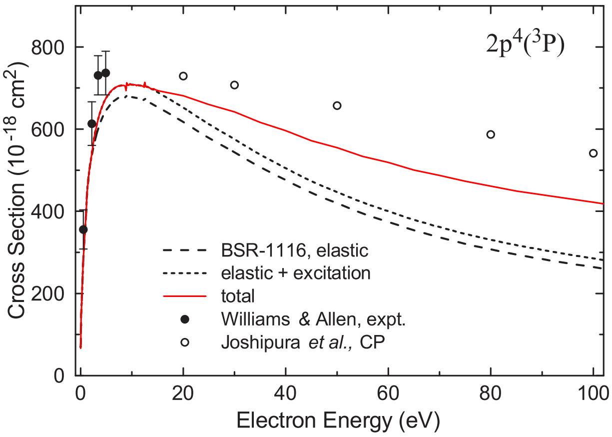

FIG. 22. Angle-integrated elastic, elastic + excitation, and grand total (elastic + excitation + ionization) cross sections for electron collisions with oxygen atoms in their $(2p^4)\,^3P$ ground state. The experimental results of Williams and Allen [29] and theoretical data of Joshupura *et al.* obtained from the complex potential (CP) method [55] have also been shown.

cross sections is needed in low-temperature plasma modeling to calculate electron swarm parameters [54].

We compare our results for the ground $2p^4\,^3P$ state with the experiment of Williams and Allen [29] in Fig. 22. The results agree closely for the lowest energy of 3.5 eV; however, for the higher energies the present total cross sections slightly underestimate the experimental values. Figure 22 also compares our total cross sections with the results from the complex energy-dependent potential derived from the atomic electron charge density [55]. These cross sections considerably overestimate our results by up to 25% at higher energies, most likely due to ignoring the initial-state correlation in their approach.

The total cross sections for the metastable ^1D and ^1S states are shown in Figs. 23 and 24, respectively. These results are very similar to the total cross sections from the ground state in magnitude as well as in shape. At low energies, they have distinctive resonance structure due to the presence of the $O^-(2s2p^6)\,^1S$ state. Deexcitation of the ^1D metastable state to the ground state has the exchange character and is negligibly small in comparison to other processes. Deexcitation of the ^1S metastable state is more important, and shows a strong narrow peak at the threshold. This would be important if there is a significant amount of metastable atoms in the system.

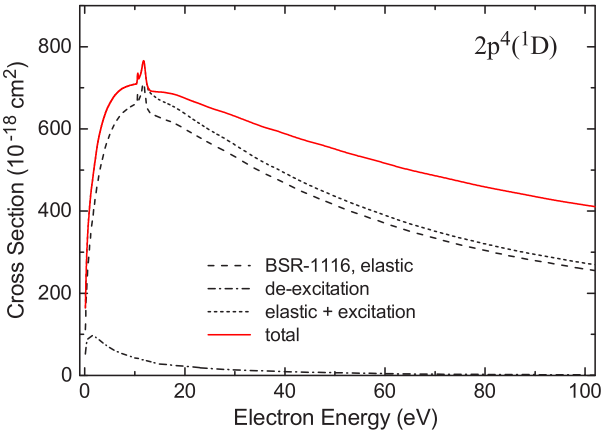

FIG. 23. Angle-integrated elastic, elastic + excitation, elastic + excitation + ionization, and grand total cross sections for electron collisions with oxygen atoms in their $(2p^4)\,^1D$ metastable state. In this case, the grand total cross sections also contain deexcitation through superelastic scattering.

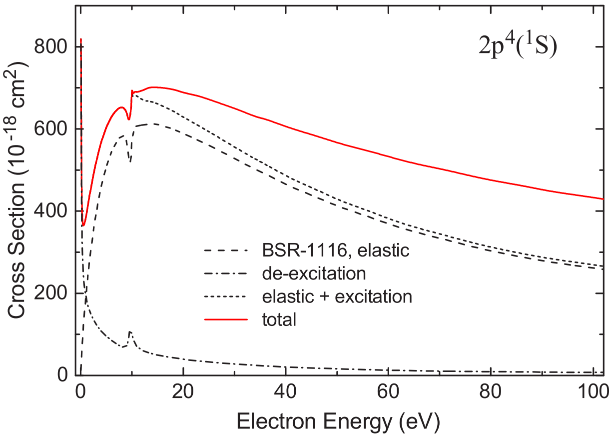

FIG. 24. Angle-integrated elastic, elastic + excitation, elastic + excitation + ionization, and grand total cross sections for electron collisions with oxygen atoms in their $(2p^4)\,^1S$ metastable state. In this case, the grand total cross sections also contain deexcitation through superelastic scattering.

IV. SUMMARY AND CONCLUSIONS

A set of cross sections for elastic scattering, electron-induced excitation, deexcitation, and ionization of atomic oxygen initially in its ground or metastable states has been presented. The calculations have been performed using the *B*-spline *R*-matrix method, where a *B*-spline basis is employed for the description of the continuum functions. The nonorthogonal orbitals have been used for the target description, which allow for high flexibility and accuracy of the target wave functions. A large number of pseudostates have been included in the close-coupling expansion in the present calculations. These pseudostates allow for the inclusion of coupling to the target ionization continuum and high-lying Rydberg states on transitions between the discrete states that are of interest in plasma modeling calculations. The *ab initio* calculation of the ionization cross sections is also made possible by the pseudostates. We have attempted to include in our scattering calculations all important physical effects including short-range correlation in the target states and long-range polarization effects in the scattering system.

Comparison of different scattering models along with the available experimental results allows us to conclude that the excitation cross sections for the transitions between all terms of the ground $2p^4$ configuration are known to an accuracy of a few percent. For these transitions the coupling to the continuum was found to have very limited influence.

The transitions to the valence $2p^3nl$ states have been found to be strongly affected by the target continuum represented by a large number of pseudostates in our calculation. The target continuum represents corrections of up to a factor of 2 for some dipole and quadrupole transitions, especially for transitions involving the $2p$-$3d$ electron promotion. In general, the $2p$-$3d$ transitions appear to be very dependent on the coupling to the target continuum for the atoms with outer p shells, and has also been noted in previous calculations for nitrogen, fluorine, and neon atoms. We used the largest possible close-coupling expansions which can be applied with modern computational resources. Though restriction on number of target states does not allow for an unambiguous conclusion about convergence, we believe that the present results should be the most accurate to date and, therefore, can be used in astrophysical plasmas modeling with confidence.

Comparison with our previous calculations [8,9] illustrates the big influence of the target continuum in the present case of electron scattering with atomic oxygen for a variety of transitions. These corrections are in line with the findings for the electron scattering on atoms with an outer $2p^n$ shell, such as C [13], N [14], F [15], and Ne [16,17]. For all these atoms the target-continuum corrections are approximately of the same order, increasing in size for atoms with a bigger occupation of the outer p shell.

We also provide a detailed comparison with the available measurements both for the direct excitation and for the emission cross sections. Most of the experimental data have large error bars and do not agree with each other. Overall, inclusion of the target continuum leads to closer agreement with the existing experimental data. This agreement, however, depends on the energy region and the transition under consideration. The theoretical cross sections for the forbidden $2p^4\,{}^3P$–${}^1D$, ${}^1S$ and $2p^4\,{}^1D$–${}^1S$ transitions appear to converge and may be considered well established at all energies. In spite of the large experimental error bars, the agreement between theory and experiment is not very satisfactory for the forbidden $2p^4\,{}^3P$–$2p^33p\,{}^3P$ and ${}^5P$ (777 nm) and spin-forbidden $2p^4\,{}^3P$–$2p^33s\,{}^5S^o$ (135.6 nm) transitions. No systematic trend of disagreement emerges with incident electron energies for these transitions. There is a reasonable agreement between the present theory and various measured values for the resonance transitions except for the $2p^4\,{}^3P$–$2p^33d\,{}^3D^o$ transition, where the present cross section agrees only at 100 eV with the experiment of Vaughan and Doering [43].

The nonperturbative calculations of ionization cross sections for the ground and metastable states of oxygen have been provided. Close agreement was obtained with the available experimental results. Electronic files for data including the complete set of excitation cross sections for all transitions between spectroscopic states indicated in Table I as well as elastic, momentum transfer, and ionization cross sections for the ground and metastable states for electron energies up to 200 eV are available from the authors upon request. We believe that we reported the most comprehensive data for the electron scattering with atomic oxygen available in the literature to date.

ACKNOWLEDGMENTS

This work was supported by NASA under Grant No. NNX11AB62G from the Solar and Heliophysics program, and by the United States National Science Foundation under Grant No. PHY-1520970, and by the XSEDE Allocation No. PHY-090031.

---

[1] M. Carlsson and P. G. Judge, Astrophys. J. **402**, 344 (1993).

[2] R. G. Athay and P. G. Judge, Astrophys. J. **438**, 491 (1995).

[3] B. C. Wolven, H. W. Moos, K. D. Retherford, P. D. Feldman, D. F. Strobel, W. H. Smyth, and F. L. Roesler, J. Geophys. Res. **106**, 26155 (2001).

[4] A. M. Amarsi, M. Asplund, R. Collet, and J. Leenaarts, Mon. Not. R. Astron. Soc. **455**, 3735 (2016).

[5] D. A. VandenBerg, P. A. Bergbusch, A. Dotter, J. W. Ferguson, G. Michaud, J. Richer, and C. R. Proffitt, Astrophys. J. **755**, 15 (2012).

[6] N. Madhsudhan, Astrophys. J. **758**, 36 (2012).

[7] P. V. Johnson, J. W. McConkey, S. S. Tayal, and I. Kanik, Can. J. Phys. **34**, 589 (2005).

[8] O. Zatsarinny and S. S. Tayal, J. Phys. B **34**, 1299 (2001).

[9] O. Zatsarinny and S. S. Tayal, J. Phys. B **35**, 241 (2002).

[10] S. S. Tayal, Phys. Rev. A **66**, 030701(R) (2002).

[11] S. S. Tayal, J. Geophys. Res. **109**, A08301 (2004).

[12] M. Plummer, C. J. Noble, and M. Le Dourneuf, J. Phys. B **37**, 2979 (2004).

[13] Y. Wang, O. Zatsarinny, and K. Bartschat, Phys. Rev. A **87**, 012704 (2013).

[14] Y. Wang, O. Zatsarinny, and K. Bartschat, Phys. Rev. A **89**, 062714 (2014).

[15] V. Gedeon, S. Gedeon, V. Lazur, E. Nagy, O. Zatsarinny, and K. Bartschat, Phys. Rev. A **89**, 052713 (2014).

[16] O. Zatsarinny and K. Bartschat, Phys. Rev. A **86**, 022717 (2012).

[17] O. Zatsarinny and K. Bartschat, Phys. Rev. A **85**, 062710 (2012).

[18] O. Zatsarinny, Comput. Phys. Commun. **174**, 273 (2006).

[19] K. A. Berrington, W. B. Eissner, and P. H. Norrington, Comput. Phys. Commun. **92**, 290 (1995).

[20] N. R. Badnell, http://amdpp.phys.strath.ac.uk/rmatrix/.

[21] O. Zatsarinny and K. Bartschat, Phys. Rev. Lett. **107**, 023203 (2011).

[22] O. Zatsarinny and K. Bartschat, J. Phys. B **47**, 061001 (2014).

[23] O. Zatsarinny and C. Froese Fischer, Comput. Phys. Commun. **180**, 2041 (2009).

[24] C. Froese Fischer, G. Tachiev, G. Gaigalas, and M. R. Godefroid, Comput. Phys. Commun. **176**, 559 (2007).

[25] A. Kramida, Yu. Ralchenko, J. Reader, and NIST ASD Team. NIST Atomic Spectra Database (ver. 5.1), http://physics.nist.gov/asd.

[26] P. G. Burke, R-*Matrix Theory of Atomic Collisions* (Springer-Verlag, Berlin, 2011).

[27] N. Badnell, J. Phys. B **32**, 5583 (1999); see also http://amdpp.phys.strath.ac.uk/UK_RmaX/codes.html.

[28] O. Zatsarinny, K. Bartschat, and S. S. Tayal, J. Phys. B **39**, 1237 (2006).

[29] J. F. Williams and L. J. Allen, J. Phys. B **22**, 3529 (1989).

[30] R. A. Alpher and D. R. White, Phys. Fluids **2**, 153 (1959).

[31] T. W. Shyn and W. E. Sharp, J. Geophys. Res. **91**, 1691 (1986).

[32] J. P. Doering, J. Geophys. Res. **97**, 19531 (1992).
[33] J. P. Doering and E. E. Gulcicek, J. Geophys. Res. **94**, 1541 (1989).
[34] S. J. Buckman and C. W. Clark, Rev. Mod. Phys. **66**, 539 (1994).
[35] J. P. Doering and S. O. Vaughan, J. Geophys. Res. **91**, 3279 (1986).
[36] S. O. Vaughan and J. P. Doering, J. Geophys. Res. **91**, 13755 (1986).
[37] S. O. Vaughan and J. P. Doering, J. Geophys. Res. **92**, 7749 (1987).
[38] E. E. Gulcicek and J. P. Doering, J. Geophys. Res. **93**, 5879 (1988).
[39] J. P. Doering and J. Yang, J. Geophys. Res. **106**, 203 (2001).
[40] I. Kanik, P. V. Johnson, M. B. Das, M. A. Khakoo, and S. S. Tayal, J. Phys. B **34**, 2647 (2001).
[41] P. V. Johnson, I. Kanik, M. A. Khakoo, J. W. McConkey, and S. S. Tayal, J. Phys. B **36**, 4289 (2003).
[42] Y. Wang and Y. Zhou, J. Phys. B **39**, 3009 (2006).
[43] S. O. Vaughan and J. P. Doering, J. Geophys. Res. **93**, 289 (1988).
[44] C. P. Ballance and D. C. Griffin, J. Phys. B **37**, 2943 (2004).
[45] E. E. Gulcicek, J. P. Doering, and S. O. Vaughan, J. Geophys. Res. **93**, 5885 (1988).
[46] J. P. Doering and E. E. Gulcicek, J. Geophys. Res. **94**, 2733 (1989).
[47] P. V. Johnson, I. Kanik, D. E. Shemansky, and X. Liu, J. Phys. B **36**, 3203 (2003).
[48] E. C. Zipf and P. W. Erdman, J. Geophys. Res. **90**, 11087 (1985).
[49] S. Wang and J. W. McConkey, J. Phys. B **25**, 5461 (1992).
[50] C. Noren, I. Kanik, P. V. Johnson, P. McCartney, G. K. James, and J. M. Ajello, J. Phys. B **34**, 2667 (2001).
[51] E. Brook, M. F. A. Harrison, and A. C. H. Smith, J. Phys. B **11**, 3115 (1978).
[52] W. R. Thompson, M. B. Shah, and H. B. Gilbody, J. Phys. B **28**, 1321 (1995).
[53] Y.-K. Kim and J.-P. Desclaux, Phys. Rev. A **66**, 012708 (2002).
[54] L. L. Alves, K. Bartschat, S. F. Biagi, M. C. Bordage, L. C. Pitchford, C. M. Ferreira, G. J. M. Hagelaar, W. L. Morgan, S. Pancheshnyi, A. V. Phelps, V. Puech, and O. Zatsarinny, J. Phys. D **46**, 334002 (2013).
[55] K. N. Joshipura, B. K. Antony, and Minaxi Vinodkumar, J. Phys. B **35**, 4211 (2002).